Initial Whirl-Flutter Characterization of the TiltRotor Aeroelastic Stability Testbed

Andrew R. Kreshock **Robert P. Thornburgh** **Matthew L. Wilbur**
U. S. Army Combat Capabilities Development Command
Army Research Laboratory
Hampton, VA, USA

Hao Kang
U. S. Army Combat Capabilities Development Command
Army Research Laboratory
Aberdeen Proving Ground, MD, USA

David J. Piatak **Martin K. Sekula**
Aeroelasticity Branch
NASA Langley Research Center
Hampton, VA, USA

ABSTRACT

This paper discusses the initial wind tunnel test of the TiltRotor Aeroelastic Stability Testbed (TRAST). TRAST is a generic tiltrotor testbed developed in collaboration between NASA and the Army. Ultimately, this test was a checkout of the model systems, functionality and familiarization, but also obtained subcritical whirl-flutter data in the terms of frequency and damping. Flutter data include two main configurations with different pitch spring stiffness, referred to as 4k and 8k, that were tested at various rotor speeds and airspeeds at the NASA Langley Transonic Dynamics Tunnel. The test included two modes of drivetrain operation: powered and windmilling. However, powered mode of operation was only conducted with the 8k pitch spring. This test reinforced the traditional knowledge of whirl-flutter trends such as flutter speed would decrease with an increase in rotor speed. The critical mode consistently being the wing vertical bending mode. The chord mode as expected was not affected by the pitch spring and was likely to go unstable at a tunnel airspeed slightly beyond the wing vertical bending mode. There were also test specific challenges such as the TRAST modal damping was more sensitive to temperature and amplitude motor than was expected. This test gathered valuable data on the baseline characterization of TRAST, how to improve the model and test practices for future wind tunnel testing. Additionally, a new more automated method for experimental subcritical damping determination based on the Stockwell transform has been demonstrated that may lead to more consistent whirl-flutter stability boundaries.

Introduction

Tiltrotor aircraft promise the benefits of both the cruise speed of turboprop aircraft and the hover capability of a helicopter, however, the top speed of a tiltrotor aircraft is limited directly or indirectly by aeroelastic stability. The U.S. Army Combat Capabilities Development Command (DEVCOM) Army Research Laboratory (ARL) in collaboration with NASA and DEVCOM Aviation and Missile Center (AvMC) have developed a new tiltrotor testbed to conduct fundamental research into an aeroelastic stability phenomenon known as whirl flutter. Whirl flutter is an instability that occurs when rotor aerodynamic loads couple with the flexibility of the wing or pylon during flight of propeller-driven aircraft and tiltrotors in airplane mode (Refs. 1–3). Whirl-flutter stability is a critical design criterion for tiltrotors because it drives the wing design to have a lower aspect ratio with thicker airfoils than may be aerodynamically optimal. Due to the critical nature of the whirl-flutter instability (potential loss of an aircraft), analysis of this phenomenon tends to be conservative and

Presented at the Vertical Flight Society's 79th Annual Forum & Technology Display, West Palm Beach, FL, USA, May 16-18, 2023.

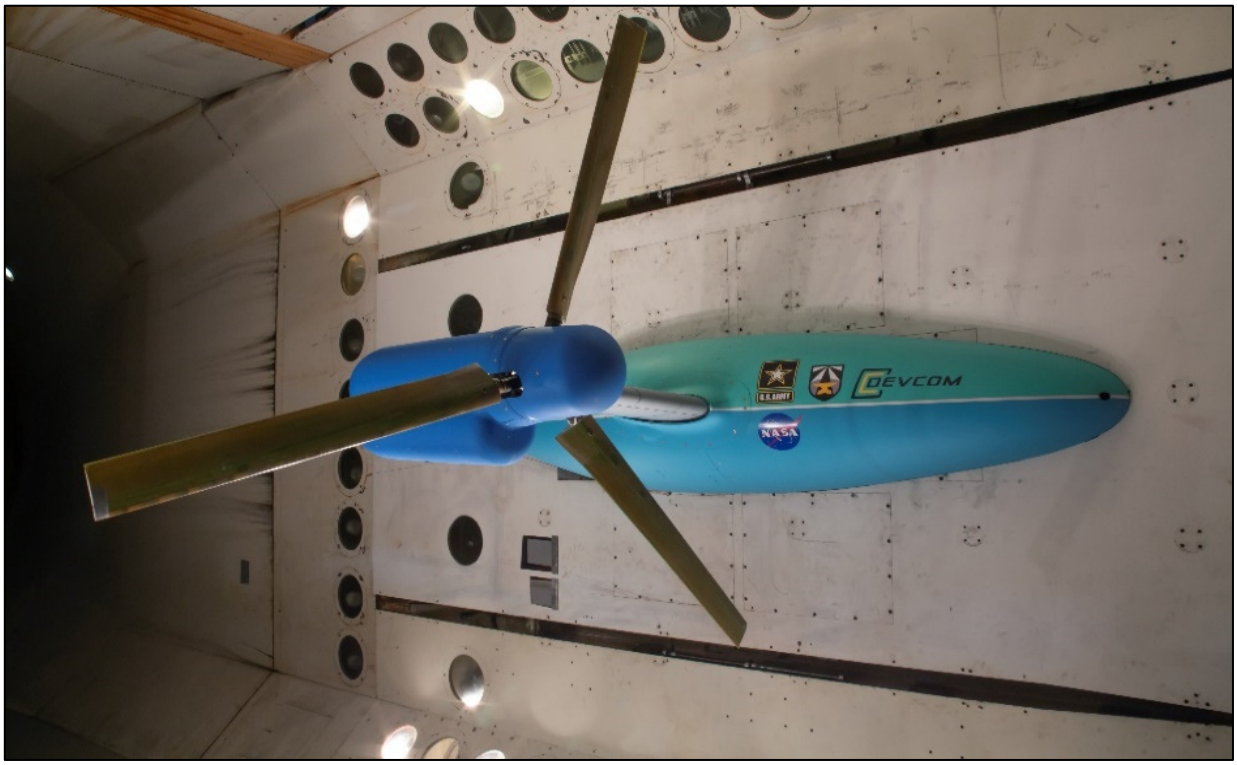

Figure 1. The TiltRotor Aeroelastic Stability Testbed in the NASA Langley Transonic Dynamic Tunnel. [Photo: NASA].

includes large safety margins on whirl-flutter speeds. One reason for this design approach is that older aircraft were designed with low-fidelity aeroelastic analyses that use simplified elements for the wing and rotor models and prescribed kinematics for the rotor dynamics. More advanced designs will require high fidelity analysis tools, which enable more accurate predictions of tiltrotor aeroelastic stability. High-quality experimental data sets are required to develop a fundamental understanding of the mechanisms contributing to whirl flutter and to validate high-fidelity analysis tools.

Table 1. Rotor and wing properties.

Rotor	Model Scale (L=0.234, ρ=1)	Notional Full-Scale Vehicle	Scale Factor
Rotor Diameter	8 ft	34.14 ft	L
Rotor Mass	6.26 lbm	487 lbm	$\rho*L^3$
Precone	2.5 deg	2.5 deg	
Max. Thrust	188 lbf	14,650 lbf	$\rho*L^3$
Wing			
Wing Length	4.4 ft	19.1 ft	L
Wing Chord	1.5 ft	6.4 ft	L
Wing Sweep (forward)	6.5 deg	6.5 deg	-
Wing Dihedral	2 deg	2 deg	-

To address this need for validation data, a semispan generic tiltrotor testbed, called the TiltRotor Aeroelastic Stability Testbed (TRAST), has been developed by the U.S. Army and NASA to investigate whirl-flutter stability of tiltrotor aircraft, and is shown in Fig. 1. The objective of the TRAST is to fill gaps in experimental data needed to support, develop, and mature new rotary-wing technologies and produce empirical data that can be used to validate tiltrotor design tools (Refs. 5–7). TRAST will be tested in the NASA Langley Transonic Dynamics Tunnel (TDT), which has a long history of testing tiltrotors with an extensive overview of previous tests in Ref 4.

Model Overview – Semispan Tiltrotor

The TRAST is a semispan model with an aeroelastically-scaled wing and 8-ft diameter rotor, shown in Fig. 2, that is designed to be tested at the TDT. This new generic testbed supersedes the Wing and Rotor Aeroelastic Test System (WRATS) that was based on the JVX 1/5th-scale aeroelastic model. WRATS testing (Ref. 8) offered many insights into the underlying physics that drove the technology development for tiltrotors, but publication of the properties of the model and experimental data generated from the test article is restricted. One of the design objectives for TRAST was to create an open and unrestricted testbed that not only reflects current tiltrotor designs but can be adapted to model new tiltrotor configurations. Thus, TRAST includes features such as interchangeable hubs, wing extensions/tips outboard of the pylon, spars, springs and tuning masses. Among them, the

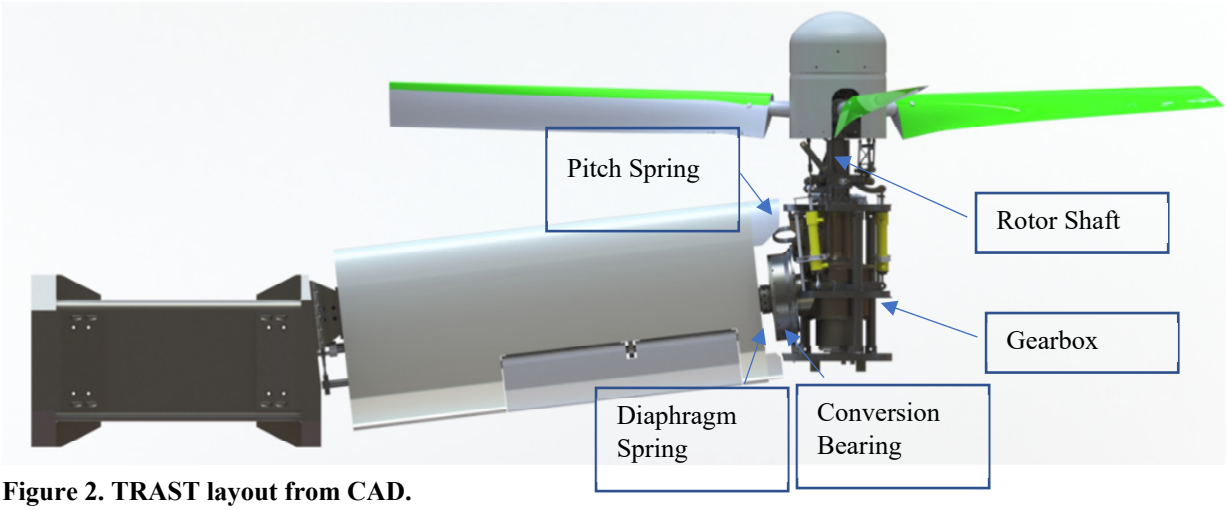

Figure 2. TRAST layout from CAD.

pylon pitch spring stiffness is one of the key parameters for TRAST whirl-flutter stability. This spring controls the pitching motion of the pylon with respect to the wingtip about the conversion axis and has values of 4,292 lb/in (4k spring) and 9,121 lb/in (8k spring). The TRAST model is loosely based on the XV-15, however, Table 1 shows how the TRAST model would compare to an ideally scaled vehicle.

TRAST is a forward-swept wing semispan model that is mounted through the wall of the test section on the sidewall turntable. The 8-ft diameter rotor is powered by a water-cooled electric motor that is located inboard of the root of the wing. The wing driveshaft has flexures that allow for the wing to bend without inducing bending moments in the driveshaft. The model has a hydraulic swashplate that is used for excitation of the wing-rotor system as well as primary rotor flight controls. The baseline model has a pitch-flap coupling angle, δ_3, of -15 degrees. The aeroelastically-scaled rotor blades are based on the XV-15 rotor design, featuring high blade twist and a constant-chord working section. The blades are instrumented with three sets of flap and lag strain gauges and two torsion strain gauges. The wing also includes three bending gauges in the vertical, in-plane and torsion directions, at three wing spanwise stations.

The TRAST was designed for analysis correlation studies and therefore has a relatively straightforward load path that can be readily modeled in structural analysis codes. The rotor is supported by a steel shaft that transmits torque, forces and moments from the hub to the gearbox. From the gearbox, the torque is transmitted through the wing drive shaft, with the other forces transmitted to the gearbox housing. The gearbox housing is the primary load-bearing structure for the pylon with all other pylon components mounted directly or indirectly to it, including the bulkheads, skin panels, and control system. Since the conversion bearing allows the pylon to rotate between helicopter and airplane mode, a pitch spring transfers the pitching moments to the diaphragm spring, whereas the other moments and forces get transmitted through the conversion bearing to the diaphragm spring. The diaphragm spring is a six-segmented disk that tunes the flexability between the pylon and the wing and is attached to the end-rib assembly of the wing.

The primary wing structure is a carbon-fiber tubular spar cantilevered from a spar support structure (see Fig. 3) that orients the wing to 6.5-deg forward sweep and 2-deg dihedral. In the hover cell this support structure is mounted directly to a backstop. When the TRAST is installed in the TDT test section, the support structure connects to the Oscillating Turn Table via a strut mount adapter that extends 29 inches out from the wall. In the TDT, a fuselage fairing covers the strut mount adapter and is attached to the adapter so that it pitches with the adapter when the wing angle of attack is changed.

Test Overview

This entry was the inaugural wind tunnel test of the TRAST model in the NASA Langley Transonic Dynamics Tunnel. As such it was largely a test of the model systems with the goal of understanding the model behavior in the wind tunnel with respect to design expectations and procedures, as well as its baseline wing/rotor dynamic and whirl-flutter characteristics. Therefore, a second wind tunnel test is planned that will explore more configurations and fix some of the model issues that will be understood by the end of this article.

The NASA Langley Transonic Dynamics Tunnel is a closed-circuit, continuous-flow, variable pressure wind tunnel with a 16-ft square test section. There are several features that make the TDT ideal for flutter testing, such as the bypass valves that can rapidly reduce the airspeed, direct viewing of the model from the control room, and protective screens that prevent debris from damaging the fan blades in the event of a model failure. Even though the TDT can utilize R-134a as a test medium, this first test entry for TRAST was conducted solely in air. In addition, the pressure was reduced to 1900 psf

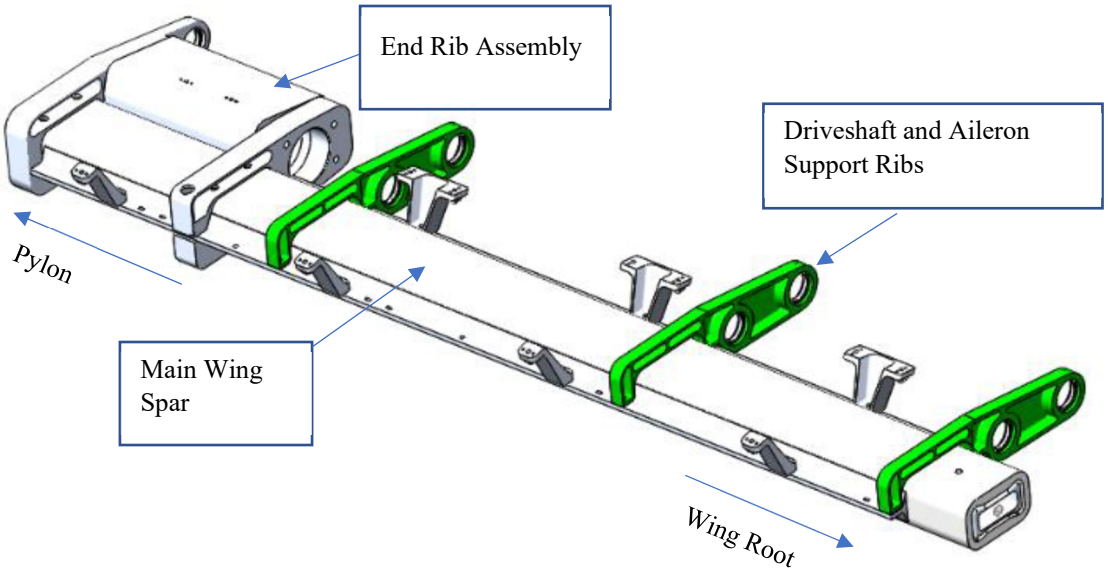

Figure 3. TRAST wing spar assembly.

to avoid overpressurizing the tunnel. The resulting air density varied between 0.0020–0.0022 slugs/ft^3 depending on tunnel temperature.

The custom TRAST data acquisition system has 24-bit resolution, and signals are filtered and amplified using an external filter-amplifier. The data system includes continuous streaming to disk, real time monitoring and pilot digital feedback. The control system for swashplate control is a digital control loop that runs on a dSPACE system that allows for changes to the pilot sensitivity and sets control limits to prevent damage to the model.

The data presented in this paper include: ground vibration modal test results, wind-off rotor performance in TDT test section, wind-on wing only (no rotor) stability results, and wind-on whirl-flutter results for two pylon pitch spring stiffnesses. During whirl-flutter testing, rotor speeds were varied from 70 to 100% Nominal Rotor speed (NR), 636-909 RPM, in 10% increments and test section airspeed was varied between 40 and 170 knots.

Ground Vibration Testing

A ground vibration test was conducted with the model cantilevered in airplane mode to a backstop prior to testing in the TDT, Fig. 4. The goal of the vibration test was to determine dynamic characteristics of the TRAST testbed and provide measured data for structural model validation. The response of the model was measured using a set of eight permanently mounted single-axis DC MEMS accelerometers mounted to the pylon structure and four triaxial piezoelectric accelerometers on the hub. The force inputs were measured using piezoelectric force transducers mounted between the shaker and the hub spinner.

There are four primary modes dominating the response of the wing-pylon system. These modes are best visualized from the modes computed by the finite element model in airplane mode, presented in Fig. 5. The vertical bending mode is similar to the first natural mode of a cantilevered beam. However, the pitch spring and the offset of the pylon center of gravity results in a significant pylon-rotation component in the mode. The second mode is wing in-plane bending that is driven primarily by the chordwise motion of the wing spar with some small contribution from the diaphragm spring. Mode 3 is the wing-torsion mode, that can be referred to as the pylon-pitch mode because the pitch spring contributes a significant amount of rotation to the mode shape. The last mode is pylon yaw and resembles a second chordwise

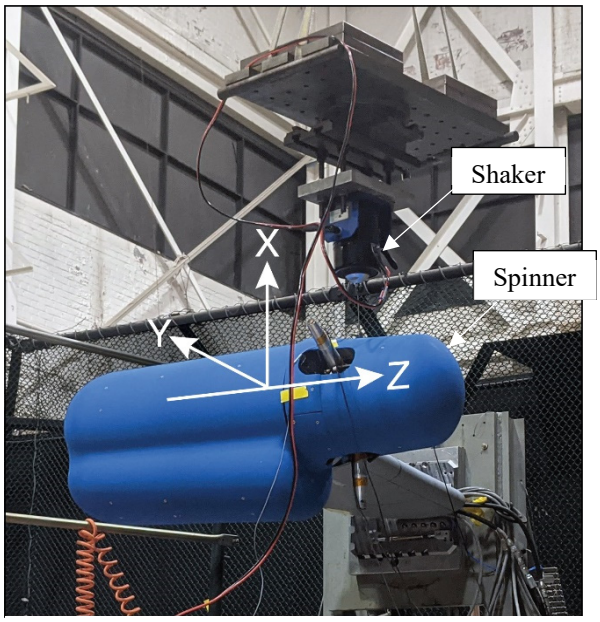

Figure 4. TRAST ground vibration testing.

Table 2. Wing-pylon measured and predicted model frequencies in airplane mode, with the 8k and 4k pitch springs, and without blades installed.

	8k Pitch Spring			4k Pitch Spring		
		NASTRAN			NASTRAN	
Rotor Mode	Measured	Rigid Boundary	TDT Tuned Stiffness	Measured	Rigid Boundary	TDT Tuned Stiffness
Wing Vertical Bending	5.36	5.47	5.34	5.23	5.38	5.26
Wing In-Plane Bending	8.35	8.55	8.29	8.20	8.54	8.28
Pylon Pitch	11.75	12.19	11.88	9.81	9.96	9.78
Aileron Pitch		14.03	14.03		14.02	14.02
Pylon Yaw	20.50	20.55	20.19	19.89	20.55	20.20
Pylon Roll		36.92	36.58		36.85	36.50

bending mode with the wing bending forward and the diaphragm spring allowing the pylon to rotate outboard. The measured and predicted frequencies for the TRAST in the wind tunnel with the 8k and 4k pitch springs are presented in Table 2.

Since the boundary condition at the wing root was shown to significantly influence the frequency response of the wing during component-level testing, it was expected that the wing mount in the TDT test section would be more compliant than the ideal, rigid boundary condition assumed in the finite-element models. The natural-frequency measurements of the TRAST without blades were used to validate the accuracy of the FEMs and identify the compliance of the model mount in the wind tunnel. The measured frequencies are distinctly lower than the NASTRAN predictions with a rigid wing-root boundary condition, as shown in Table 2. Consequently, an elastic joint was added to the model at the wing root to simulate the TDT mount stiffness, and the stiffness was tuned so that the predicted modal frequencies agreed with the measured values. All of these comparisons have been documented in a NASA Technical Memo under review for publication (Ref. 9–10).

The NASTRAN model was then used to determined mode shapes at the hub node for the wind tunnel predictions that are listed in Tables 3 and 4. Both mode shapes are normalized to a unit modal mass (slinches) with a point mass representing the rotor mass. In a comprehensive model, this rotor mass representation typically implies that the mass of the FEM rotor will be subtracted, depending on the modeling details.

Table 3. NASTRAN Mode shape at the hub node for the TRAST model with the 4k (4,292 lb/in) pitch spring installed with concentrated rotor mass at hub node.

Mode Shapes	Freq (Hz)	X (in/in)	Y (in/in)	Z (in/in)	rX (rad/in)	rY (rad/in)	rZ (rad/in)
Wing Vertical Bending	5.02	2.62E+00	1.82E-01	-8.28E-03	-3.29E-03	5.22E-02	7.76E-04
Wing In-plane Bending	7.92	-2.50E-01	1.72E+00	1.80E+00	-9.57E-02	-2.01E-02	-1.50E-04
Wing Torsion	9.26	-2.60E+00	-4.35E-01	-1.81E-01	3.09E-02	-2.27E-01	-2.67E-03
Pylon Yaw	18.69	-3.32E-01	3.28E+00	-6.37E-01	-2.10E-01	-2.33E-02	-7.61E-05

Table 4. NASTRAN Mode shapes at the hub node for the TRAST model with the 8k (9,121 lb/in) pitch spring installed with concentrated rotor mass at hub node.

Mode Shapes	Freq (Hz)	X (in/in)	Y (in/in)	Z (in/in)	rX (rad/in)	rY (rad/in)	rZ (rad/in)
Wing Vertical Bending	5.13	2.37E+00	1.64E-01	-5.49E-03	-1.79E-03	3.24E-02	5.35E-04
Wing In-plane Bending	7.92	1.44E-01	-1.73E+00	-1.80E+00	9.70E-02	9.86E-03	2.88E-05
Wing Torsion	11.13	-2.84E+00	-3.94E-01	-9.08E-02	2.84E-02	-2.35E-01	-2.72E-03
Pylon Yaw	18.69	3.55E-01	-3.28E+00	6.36E-01	2.10E-01	2.52E-02	9.62E-05

Table 5. 4k Pitch Spring versus 8k Pitch Spring without blades.

Mode	4k Pitch Spring		8k Pitch Spring	
	Frequency (Hz)	Damping (%)	Frequency (Hz)	Damping (%)
Wing Vertical Bending	5.23	0.74	5.36	0.53
Wing In-plane Bending	8.20	0.87	8.35	0.67
Wing Torsion/Pylon Pitch	9.81	4.4	11.75	4.60
Wing 2nd In-plane/Pylon Yaw	19.89	1.46	20.5	1.16

Figure 4 shows the orientation of the coordinate system for both the vibration test and the NASTRAN mode shapes.

An important objective of the ground vibration testing for flutter analysis, is the characterization of the modal structural damping. The structural damping adds a component to the damping that can drastically change the conditions at which a particular mode will go unstable. The damping was determined using a process similar to that used during the wind tunnel test. The TRAST model was physically excited, and the moving-block method was used to determine the frequency and damping from the time history of the free decay response. Table 5 presents the measured frequency and damping of the TRAST model with the 4k and 8k pitch springs installed. The 4k pitch spring has approximately 0.2% more damping across all modes compared to the 8k pitch spring. Damping increases when the blades are installed in the model, as seen in the results presented in Table 6. This damping increase occurs primarily in the wing vertical bending and yaw modes, and to a lesser degree in the wing in-plane and torsion modes. This increase in damping of the wing vertical mode is attributed to friction in the gimbal joint. This friction is both amplitude and temperature dependent, but in general, the wing vertical bending mode damping was approximately 2.2% under normal operating conditions (an increase of 1.5% from without blades). At extremes (cold model and high amplitude) the measured damping would increase to as large as 3.5%. This temperature and amplitude dependency is a serious issue and steps have been taken to mitigate its source for future tests. Similar increase in damping can be observed when the 8k pitch spring is installed.

Cantilevered vibration testing was conducted on the individual rotor blades to validate the accuracy of the structural blade model without the complication of the hub and the rest of the wing and pylon system. To cantilever the blades, a dummy pitch case was used that mounted them to a floor

Table 6. 4k Pitch Spring with blades.

Mode	4k Pitch Spring	
	Frequency (Hz)	Damping (%)
Wing Vertical Bending	5.05	2.3
Wing In-plane Bending	7.69	0.7
Wing Torsion/Pylon Pitch	10.6	5+
Wing 2nd In-plane/Pylon Yaw	18.5	3.5

Table 7. Rotor blade frequencies for cantilevered blades.

Mode, Hz	White	Green	Red	Blue
Mass, lbm	1.622	1.606	1.620	1.626
1st Flap	15.44	15.00	15.92	15.53
1st Chord	32.77	33.60	32.99	33.77
2nd Flap	62.70	61.77	64.88	63.25
3rd Flap	144.6	143.2	148.8	146.1
1st Tors.	170.9	167.7	171.8	169.1

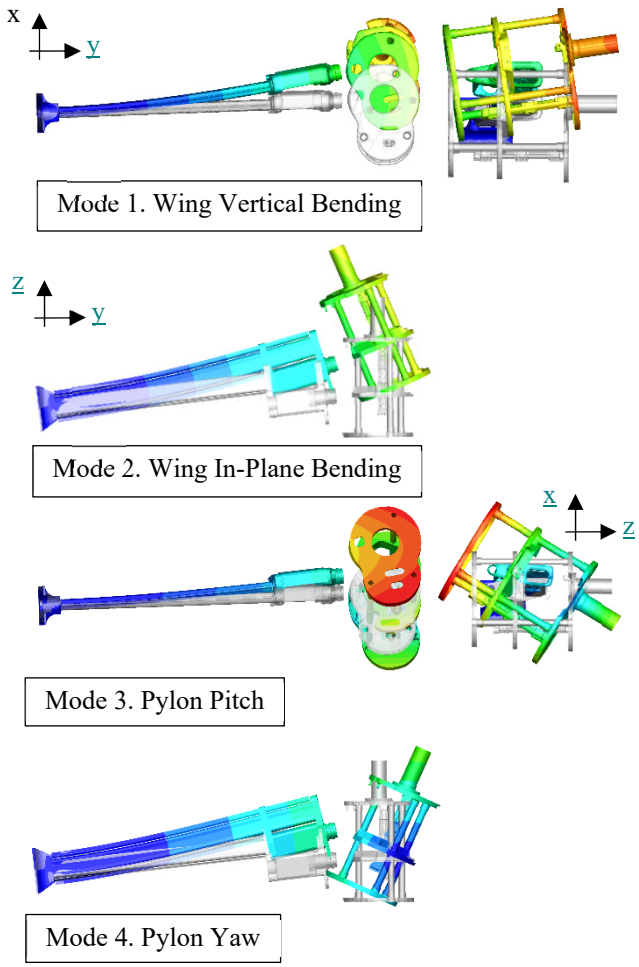

Figure 5. Mode shapes from finite-element model in airplane mode.

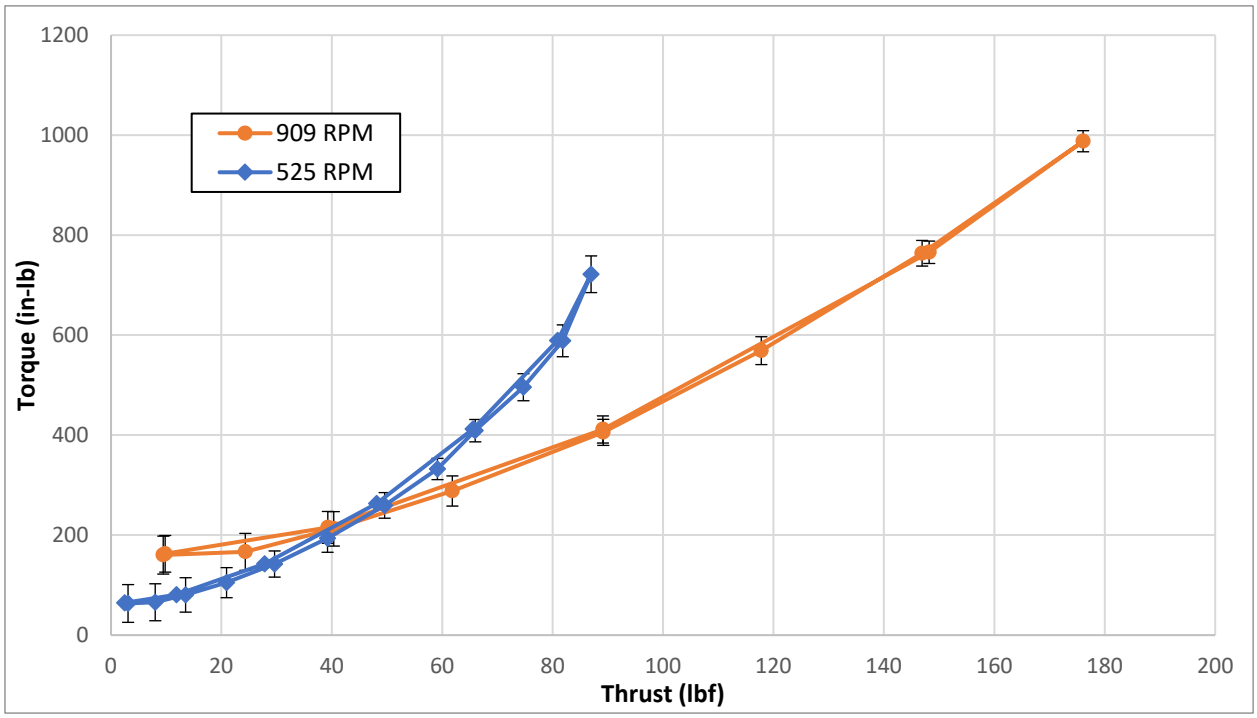

Figure 6. Rotor torque versus thrust in airplane mode in the TDT test section.

fixture. The measured frequencies for each of the blades are presented in Table 7. The blades were color coded based on the color of the embedded LED in the tip of the blade for tracking. The three chosen for wind tunnel testing, white, red and blue, were selected primarily based on similar blade mass.

Rotor Performance

Rotor performance was validated by performing a collective pitch sweep with the model in airplane mode. However, being an aeroelastic model a balance was not installed in the model due to the weight and dynamics associated with them. However, in airplane mode the loads due to the interaction of the rotor wake with the wing are small and therefore the root bending gauges can be used to estimate the thrust of the rotor. Figure 6 shows the measured torque versus the estimated thrust for the collective sweep for rotor speeds of 525 RPM and 909 RPM.

Excitation and Damping

An established approach to measuring system damping of a tiltrotor wind-tunnel model has been adopted in the present work, where the rotor control system is used to excite the model near the wing/pylon modal frequency of interest and the free decay of the model response is measured. The TRAST hydraulic swashplate control system can provide consistent excitation up to a frequency of 25 Hz. Swashplate actuation changes the blade pitch in a manner that produces rotor oscillatory aerodynamic forces that excite the model modes near that actuation frequency. Once the model is excited, strain gauge and accelerometer responses are acquired. Figure 7 presents a sample of this model excitation and free decay with the blue line indicating the excitation amplitude and the black line the model response to this input, with the highlighted portion being the free-decay response that is analyzed for damping. Each time history is analyzed using both moving-block and Prony methods, two proven algorithms for calculating damping (Ref. 11). One of the problems with this experimental approach to determine damping is that, in high-speed forward flight, the free-stream turbulence excites the model response. This external excitation, combined with the low damping in this flight regime, results in significant scatter in the damping results.

The damping for any particular time history for this model was dependent on the time segment analyzed, in addition to the turbulence. The results presented in Fig. 8 demonstrate the variation in damping determined using the moving block method as the window of the damping fit analysis is adjusted. Initially the damping was found to be 3.357% at the start of the decay, but by the end of the decay it had increased to over double that value to 7.179%. This wide range of damping can partially be attributed to friction in the hub and conversion bearing. To address this issue in the next wind tunnel test, steps are being taken to remove some of this friction, thereby eliminating some of this time-varying behavior. It should be noted that the ripples in the amplitude vector are a result of the moving block process using a Discrete Fourier Transform (DFT) of a decaying sine wave. Although a simple Hanning window can remove this effect, it can skew amplitude due to windowing weights.

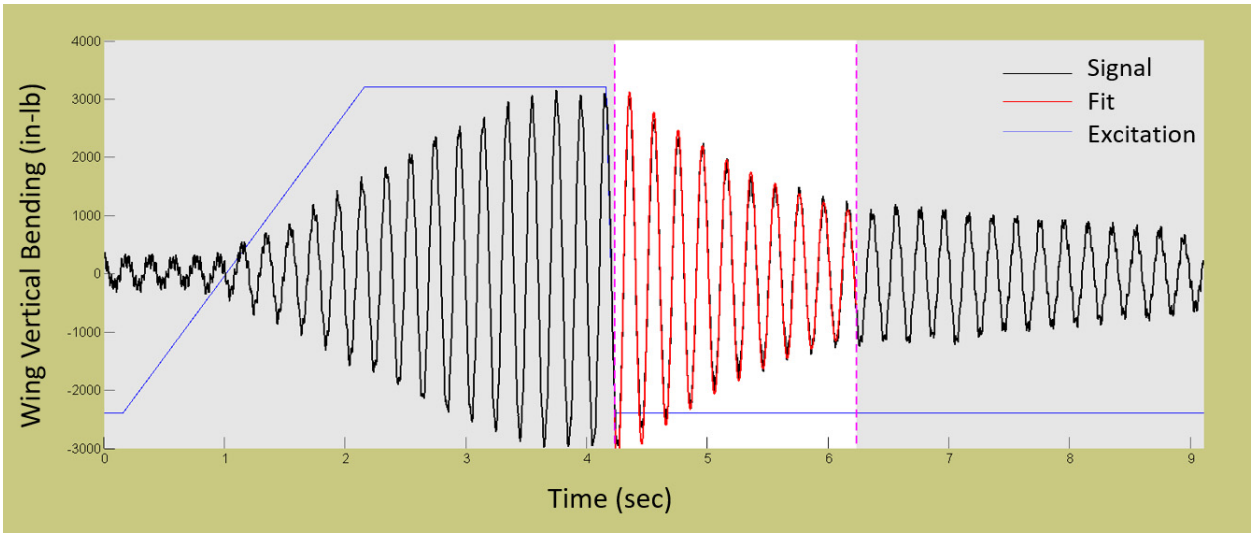

Figure 7. Sample of model excitation and free decay for the wing vertical bending gauge (in-lb) at the first wing vertical bending mode, signal history in black and curve fit from moving block in red.

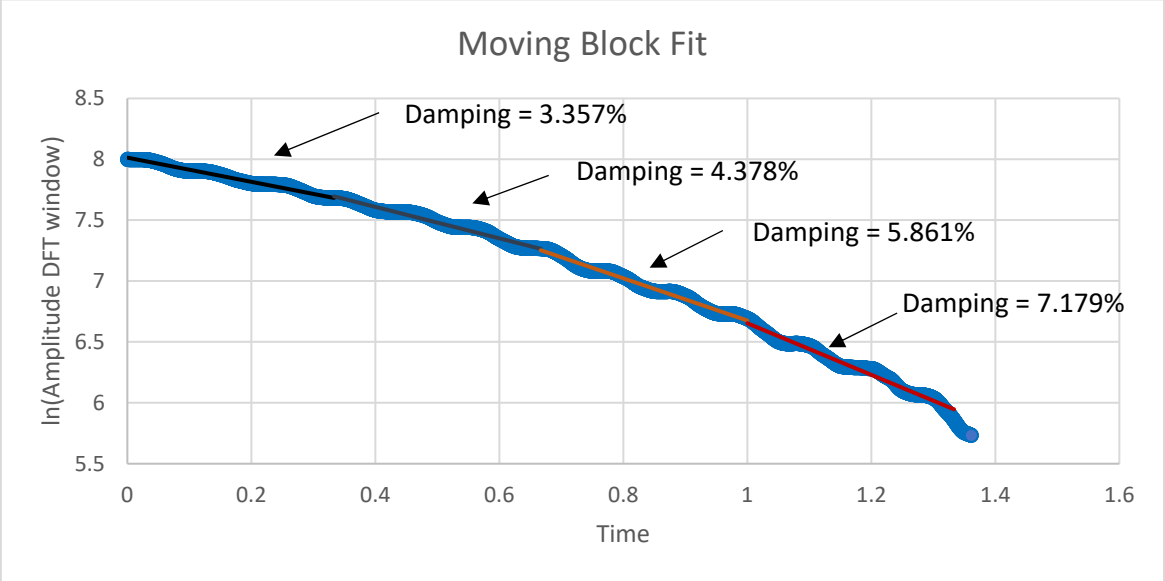

Figure 8. Log of the DFT amplitude from moving block algorithm with damping at various points in time.

Another method that is well suited to analyze a time varying signal is the Stockwell transform. The Stockwell transform, or S-transform, is a nonstationary signal analysis technique that provides a temporally-localized spectral content of a signal. The transform is based on the wavelet transform, utilizing a Gaussian mother wavelet function modified to include a phase correction factor (Ref. 12). Recently, the S-transform has been applied to analyze the dynamics of a variable speed rotor, extracting time-varying frequency content, signal-to-signal phase (as a function of time and frequency), and damping ratio of the system based on post-resonance response decay (Ref. 13). One of the most useful attributes of this transform for the present analysis is that averaging the S-transform in time collapses it into a Fourier transform of the signal. Therefore, the output of the transform is more easily interpretable, since it relates to a traditional Fourier transform. Like the Fourier transform, the amplitude response of the S-transform is frequency invariant, requiring no special frequency-related considerations.

Wind tunnel-acquired whirl-flutter data set is a good candidate for analysis with the S-transform, since each data record is a transient signal consisting of two segments: a system excitation segment, where a swashplate input is used to induce model response at a specific modal frequency, followed by a free response segment, where the model motion is allowed to decay due to the system's structural and aerodynamic damping. A sample time history of the wing vertical bending moment is provided at the bottom of Fig. 9 with the S-transform time-frequency representation (TFR) of that signal is

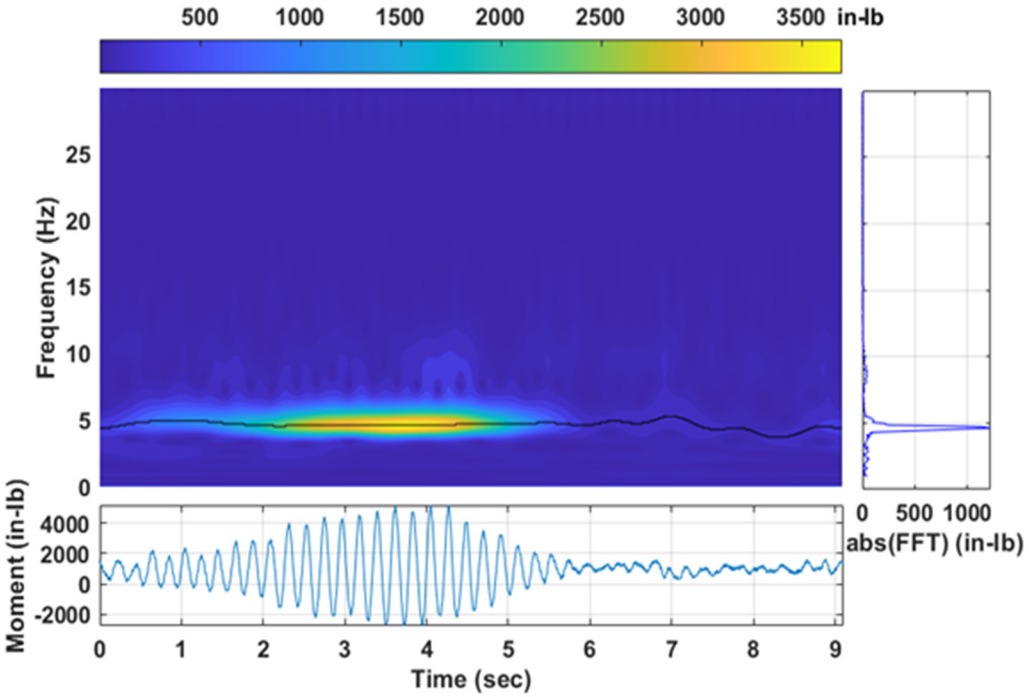

Figure 9. Stockwell-transform time-frequency representation of the wing vertical bending response due to excitation (black trace represents local maximum response).

provided above the time history. The abscissa and ordinate of the TFR represent time and frequency, respectively, while the color intensity indicates the S-transform amplitude. To the right of the figure is the time-average of the entire TFR that represents the spectral amplitude based on the entire time history that is mathematical equivalent to an FFT.

Wing-Pylon Testing (No Rotor)

Prior to testing the TRAST with the rotor installed, a wind-tunnel velocity sweep was performed with the wing and pylon, but without rotor blades and with the drive system operating at 909 RPM. This velocity sweep verified wing stability and quantified the loads that were associated with the wing and pylon aerodynamics rather than the rotor. The TRAST wing uses an asymmetric airfoil, and thus produces lift at the 0-deg angle-of-attack model attitude used during the entire wind-tunnel test. This lift, combined with the aerodynamic drag of the wing and pylon resulted in static wing-bending loads on the model that were proportional to the dynamic pressure. The relationship between dynamic pressure and the sensor outputs is presented in Table 8, based on a linear curve-fit analysis of the measured mean load.

In addition to wing bending, a small pitch-up moment on the pylon was also observed, resulting in a velocity-dependent tension in the pitch-spring in addition to 3.58 lbf of tension induced by the torque of the drive system at 909 RPM. From the chordwise bending moment at the wing root, a wing-pylon drag of 0.588 lbf/psf can be approximated assuming the 45.6 inch offset from the wing root gauges.

There were also significant oscillatory loads measured on the wing-pylon. The primary contributors to these unsteady loads were the turbulence in the tunnel airflow discussed above and 1/rev vibration from imbalance in the spinning hub. The magnitude of the response induced by the turbulence was observed to be proportional to dynamic pressure. Dynamic excitation of the model during this test showed that the modal frequencies of the system did not change significantly with increasing tunnel speed unlike the whirl-flutter cases that will be shown later. A discrete Fourier transform was performed on the steady-state wing-pylon measurements at the measured frequency of the vertical bending mode, and the results were compared to steady-state measurements with the rotor installed. The ratio of the magnitude of this modal response to the dynamic pressure is presented in Table 9. It was observed that the oscillatory responses for the wing-pylon without the rotor were comparable to the magnitudes observed with the rotor installed. This implies that the

Table 8. Relation between measured loads and dynamic pressure.

Channel	Slope	Units
Vertical Bending at Wing Root	21.21	in-lb/psf
In-plane Bending at Wing Root	-26.82	in-lb/psf
Wing Vertical, 23 inches	10.55	in-lb/psf
Wing In-plane, 23 inches	-20.42	in-lb/psf
Wing Vertical, 32 inches	6.5	in-lb/psf
Wing In-plane, 32 inches	-17.23	in-lb/psf
Pitch-Spring	0.120	lbf/psf

Table 9. Amplitude of the wing-vertical mode oscillation induced by tunnel turbulence at 909 RPM and normalized by dynamic pressure.

	No Blades 8k	Powered 8k	Windmill 8k	Windmill 4k
Vertical Bending at Wing Root (in-lb/psf)	27.0	15.0	28.2	14.7
Pitch Spring (lbf/psf)	0.523	0.403	0.630	0.485
Pylon Vertical Acceleration (in/s^2/psf)	1.97	0.85	1.55	0.67

random system response affecting the damping measurements is driven by the turbulence interaction with the wing and pylon, as opposed to the rotor. The rotor, however, does affect system damping, which results in smaller oscillation magnitude during some test conditions, particularly with the rotor powered.

Whirl-Flutter Test Results

Whirl flutter is not an easily predicted phenomenon because it is affected by the wing dynamics, the rotor dynamics and aeromechanics. Thus, there was a significant level of uncertainty in the exact airspeed of the flutter boundary prior to the test. With the primary goal of ensuring model system safety and familiarization, the test campaign started with the 8k configuration and a δ_3 = -15 deg for the rotor control system. Furthermore, the rotor was powered with the motor to precisely control rotor speed while testing. This configuration has been consistently found to be the most stable in previous tests and was chosen accordingly. Subsequent configurations were tested with decreasing levels of stability. First involved switching to a windmilling configuration, followed by switching to the softer 4k pitch spring.

Whirl-flutter testing is conducted by experimentally measuring the frequency and damping of the fundamental wing and pylon modes. This critical phenomenon is always tested in airplane mode, which is known to be the least stable configuration. To ensure accurate results, the rotor is tracked and balanced prior to commencement of testing, which helps to reduce vibration.

The test was divided in two phases. The first, powered phase used the motor to set rotor speed and then the pilot adjusted the collective to achieve the desired torque with the rotor trimmed to zero cyclic flapping angle by adjusting the cyclic pitch. The second is the windmilling condition, where the TRAST model driveshaft is disconnected at the root of the wing. This configuration is typically the most conservative (lowest stability boundary) for whirl-flutter testing. During windmilling operations, collective pitch is used to set rotor speed to desired set-points and again the cyclic flapping is trimmed to zero. In both approaches, the wind-tunnel airspeed is set to a specified value by the tunnel operators, rotor speed is set by a pilot, and swashplate excitation is applied to induce a model response used to determine the subcritical damping of the wing and pylon modes. At each tunnel airspeed and rotor speed combination, damping and frequency set of measurements (minimum of three) were taken for each of the four primary wing modes (wing vertical, wing in-plane, torsion and pylon yaw). However, the torsion mode was heavily damped during the test, limiting the ability to extract the frequency and damping accurately. Once data are recorded, the process is repeated at the next set of conditions.

The data sets from the test have been assembled into a database of test points that indicate the frequency and damping at each set point. The figures presented in this paper provide the mean damping and frequency with error bars that indicate one standard deviation across the different measurements, therefore, these values are not necessarily the true damping levels as the extracted damping would often have some variance due to factors previously discussed. In hindsight, more data would provide a better statistical confidence to the data, but the time associated with excitation and free decay measurements for four modes across four rotor speeds limited the number of repeat measurements that could be performed.

Powered Testing with 8k Pitch Spring

Powered testing was conducted by trimming to 300 in-lb of torque for each tunnel airspeed. The rotor was trimmed to torque rather than thrust since TRAST does not have a balance to accurately measure thrust. The first case discussed is the model with the 8k pitch spring installed and the rotor operating at 727 RPM (80% NR). These results, presented in Figure 10 show how the damping and frequency change versus airspeed for the four primary modes discussed above – wing vertical bending, wing in-plane, wing torsion and pylon yaw. In general, the error in the damping measurements increases in proportion to the tunnel speed. Some of this increase is due to the turbulence, which would excite the model and disrupt the free decay, but other measurement inconsistencies seem to be due to nonlinearities associated with the model. For the entire set of data, both the wing torsion and pylon yaw modes were highly damped, with the wing torsion mode in excess of 5–10% damping, while the pylon yaw mode would consistently exhibit around 4–6% damping. Due to these high damping values, both modes will be omitted from further plots. In terms of accuracy, the measured frequency was a very consistent parameter regardless of the scatter observed in the damping. The wing vertical mode has

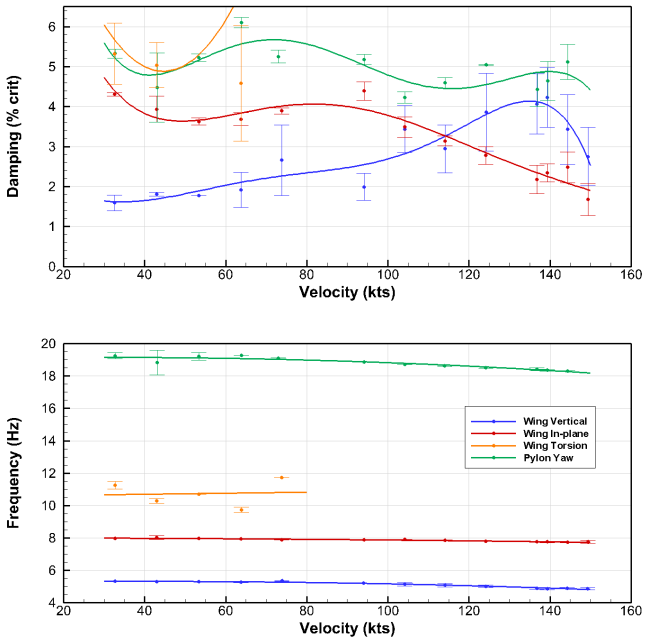

Figure 10. Frequency and damping versus tunnel airspeed for the first four primary modes, rotor speed of 727 RPM and 8k pitch spring.

a frequency that decreases from 5.33 Hz at 33 knots to 4.87 Hz at 150 knots. This decrease in frequency is very typical of whirl flutter and indicates that the rotor is aeroelastically coupling with the wing structure.

Figure 11 and 12 present comparable frequency and damping plots for rotor speeds of 818 RPM (90% NR) and 909 RPM (100% NR) for both the wing vertical and wing in-plane bending modes. Both plots are very similar with the wing in-plane mode trending towards instability. Both figures show a sharp increase in the wing in-plane damping around 70–80 kts, which is often an indication that the rotor regressive lag mode is crossing the wing in-plane mode. The wing vertical bending mode was still very stable during this powered testing with the regressive lag mode crossing likely occurring around 140 knots. At the highest tunnel airspeeds the wing vertical bending mode damping is decreasing but still in excess of 2% damping and very stable.

Torque Sweeps

Another phenomena that has been observed during prior whirl-flutter testing is that stability increases as thrust/power increases. This increase in system damping was originally demonstrated in early tiltrotor work in Ref. 14 with thrust sweeps on the rotor system. The damping being proportional to rotor thrust/power could be from a number of reasons, from the change in inflow through the rotor disk to increased loads and therefore increases the friction in various joints. Figure 13 and 14 present some typical results of the damping and frequency of the wing vertical bending mode as a function of torque for various tunnel airspeeds at 727 RPM. There was a change in the damping of approximately 2% from a torque of 50 in-lb to 500 in-lb (approximately 100 lb thrust change) in the low speeds cases. In addition, the frequency changed from 5.3 to 5.18 Hz (Δf=0.12 Hz) for the same condition. The higher speed test data did not show as clear a trend but the highest torque had, on average, higher damping than the lowest torque but with a larger variation in the measured damping.

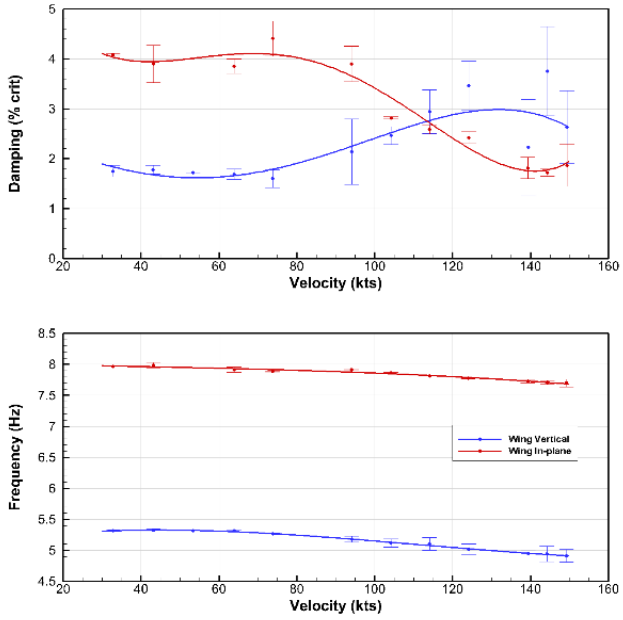

Figure 11. Frequency and damping versus tunnel airspeed, rotor speed of 818 RPM and 8k pitch spring.

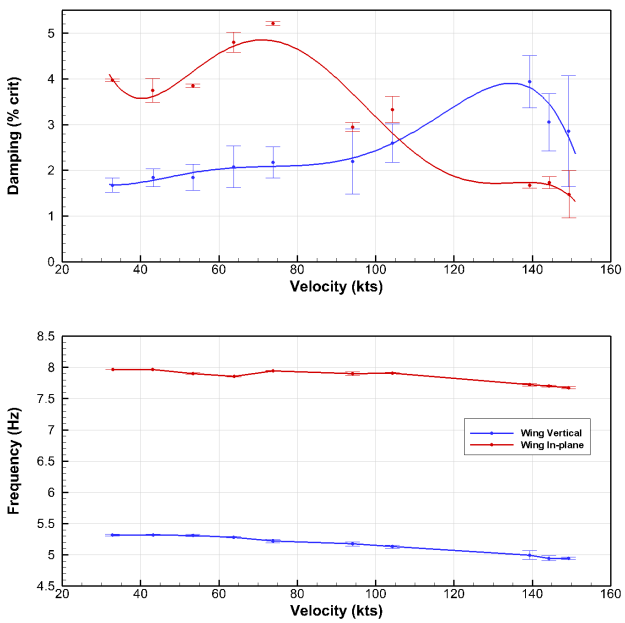

Figure 12. Frequency and damping versus tunnel airspeed, rotor speed of 909 RPM and 8k pitch spring.

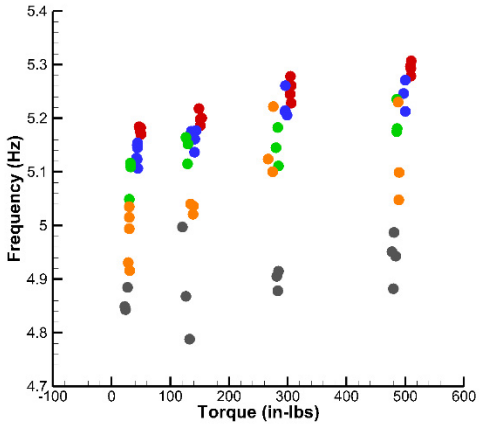

Figure 13. Frequency versus Torque for the wing vertical bending mode, rotor speed of 727 RPM and 8k pitch spring.

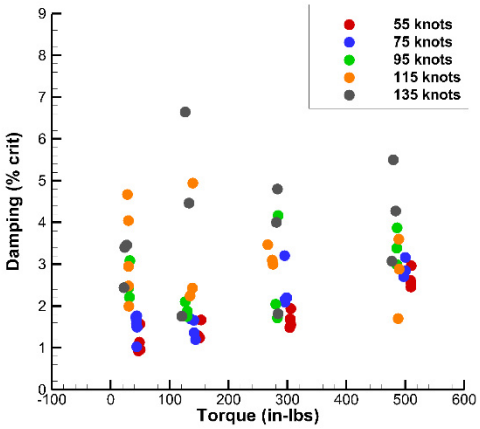

Figure 14. Damping versus Torque for the wing vertical bending mode, rotor speed of 727 RPM and 8k pitch spring.

Windmilling with 8k Pitch Spring

A windmilling wind tunnel model configuration is often employed to identify the critical flutter condition for tiltrotor aircraft. As discussed above, the rotor thrust induces more load through the hub components, which causes more friction in the rotor gimbal joint. Even without this friction, higher inflow through the rotor system should result in higher damping in the rotor. When tested in the windmilling condition, the drop in damping for this model was not as drastic as the decrease in damping observed in Ref. 8. However, this dissimilarity in behavior likely reflects the differences in the drive train configuration. During the windmilling condition for TRAST, only the motor is decoupled and the gearbox and drive shaft continues to spin with the rotor and induce damping. Conversely, the system tested in Ref. 14 plausibly has more damping introduced within the drive system, which decreases the windmilling damping even more. The drivetrain friction in the TRAST rotor system results in a constant torque of approximately -22 in-lbs. This negative torque is largely independent of the rotor speed and is sensitive to the gearbox temperature. Thus, the importance of drivetrain dynamics and damping on whirl-flutter stability is reinforced.

Figures 15 and 16 compare TRAST damping and frequency for the powered trimmed case (torque = 300 in-lb) and the windmilling case. These data illustrate again that windmilling

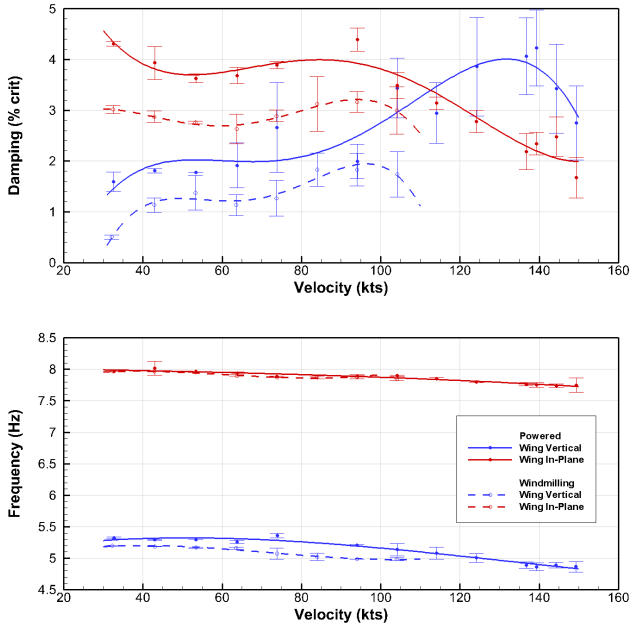

Figure 15. Damping and frequency versus tunnel airspeed, windmilling (dashed) versus powered (solid) at a rotor speed of 727 RPM and with the 8k pitch spring.

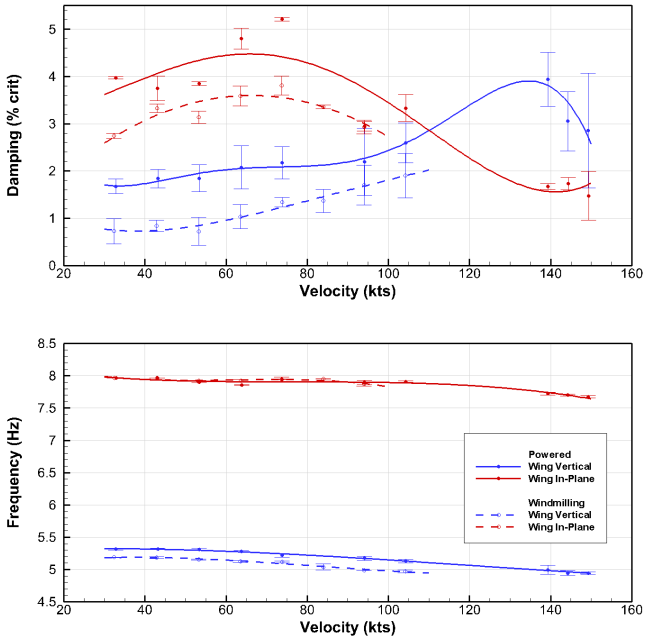

Figure 16. Damping and frequency versus tunnel airspeed, windmilling (dashed) versus powered (solid) at a rotor speed of 909 RPM and with the 8k pitch spring.

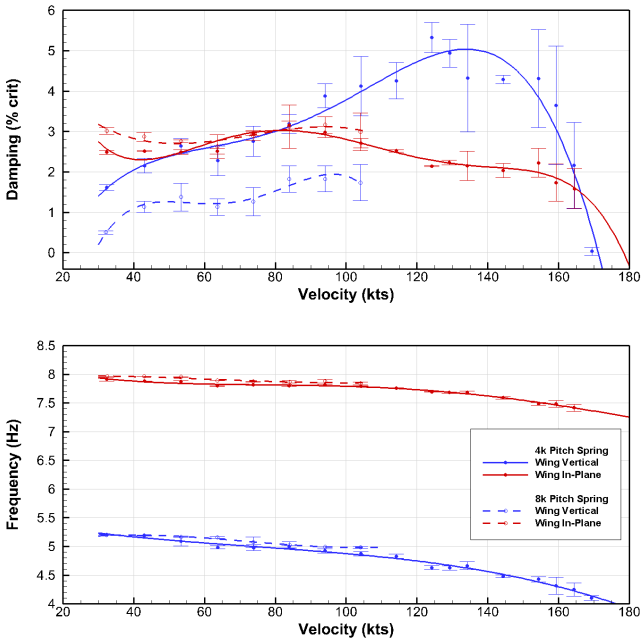

Figure 17. Wing vertical and in-plane bending frequency and damping for windmilling at a rotor speed of 727 RPM, 4k pitch spring (solid line) and 8k pitch spring (dashed line).

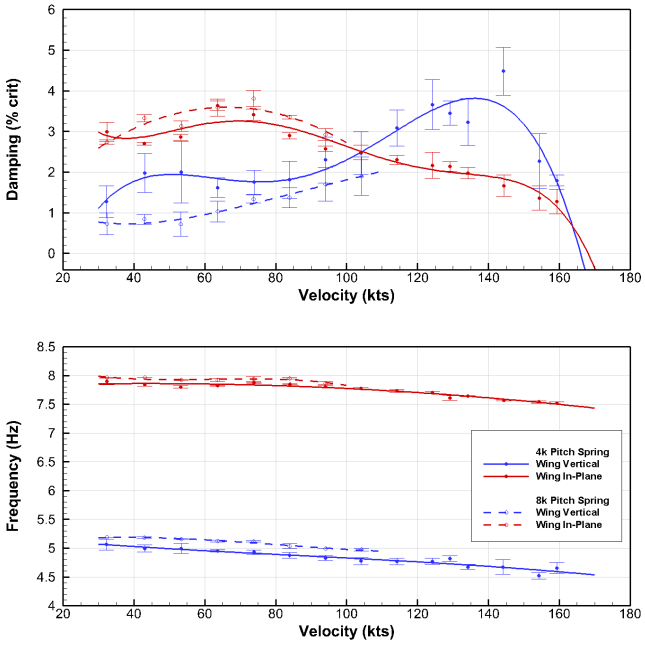

Figure 18. Wing vertical and in-plane bending frequency and damping for windmilling at a rotor speed of 909 RPM, 4k pitch spring (solid line) and 8k pitch spring (dashed line).

is less damped than the powered case, with a consistent 1% lower damping across the airspeed range. Another interesting note is that the wing vertical bending mode frequency shifted by 0.1–0.2 Hz while the wing in-plane bending mode did not. This difference is not due to a change in mass but purely a result of the change in the wing drive shaft boundary condition. The current study stopped the tunnel airspeed before the flutter boundary was obtained but it likely resembles the powered study except shifted by 1%. The 8k pitch spring testing was limited by time and other constraints placed on the current study.

Windmilling with 4k Pitch Spring

The softer, 4k (4,292 lbf/in) pitch spring was expected to result in the model going unstable at a lower flutter speed than the 8k pitch spring. Experimental results in Fig. 17 present the damping and frequency for the wing vertical and in-plane modes for the previously presented 8k pitch spring and the 4k pitch spring at 727 RPM. In practice the TRAST model with the 4k pitch spring had higher damping at low speeds, and since the 8k pitch spring was not tested to flutter it is uncertain which would flutter at the lowest airspeed. This increase in damping is likely caused by more motion induced from the softer 4k pitch spring in the conversion bearing. For the 4k pitch spring there is a large increase in damping between 130–160 kts that is associated with the rotor regressive asymmetric (cyclic) lag mode crossing the wing vertical bending mode (same crossing seen in the 8k powered testing). Around 170 kts the model was observed to be neutrally stable, and this is considered the flutter boundary at 727 RPM.

Similar experimental results are presented in Fig. 18 at a higher rotor speed of 909 RPM, which again demonstrates that the 8k pitch spring resulted in lower damping for the wing vertical bending mode. The wing in-plane mode exhibited similar trends for both the 4k and 8k pitch spring, indicating that the pitch spring has little impact on that

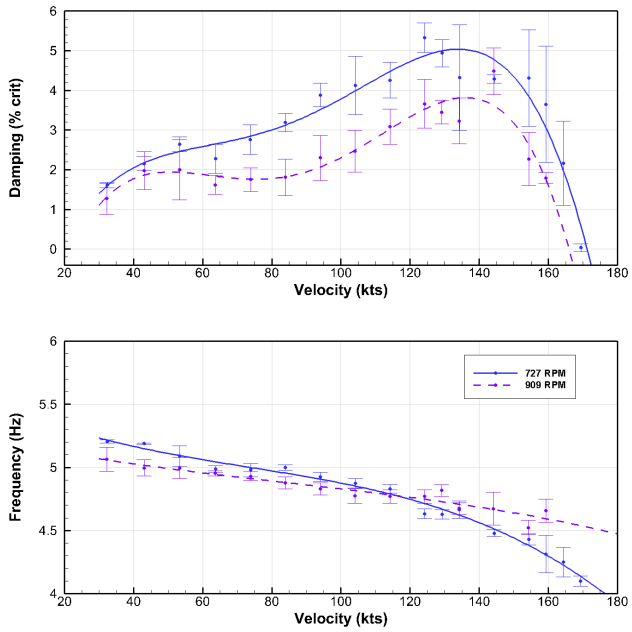

Figure 19. Wing vertical and in-plane bending frequency and damping for windmilling, 742 RPM (solid line) and 909 RPM (dashed line), with the 4k pitch spring.

particular mode. At a rotor speed of 909 RPM, the wing vertical bending mode was trending towards instability around 165 kts based on the curve fit.

Experimental results presented in Fig. 19 compare the rotor speed of 727 RPM to 909 RPM for the wing vertical bending mode. This figure again shows the classical trend that a higher rotor speed will decrease the damping of the wing vertical bending mode, although for this model configuration there appears to be only a 5 kts difference in the stability boundary between the two rotor speeds. The wing vertical bending frequency for the 909 RPM case is less affected by changes in the wind tunnel airspeed compared to the 727 RPM case.

Automated Damping Analysis using Stockwell Transform

As previously discussed, wind tunnel-acquired whirl-flutter data set is a good candidate for analysis with the S-transform, since each data record is a transient signal. Initially, a swashplate input induces model response at a specific modal frequency, followed by a free response of the model where its motion is allowed to decay due to the structural and aerodynamic damping of the system. A sample time history of the wing chordwise bending moment due to a yaw mode excitation is presented in Fig. 20a, while the S-transform time-frequency representation (TFR) of that signal is provided in Fig. 20b. The abscissa and ordinate of the TFR represent time and frequency, respectively, while the color intensity indicates the S-transform amplitude.

There are several features of note in this TFR. First, the strongest signal occurs between 18 and 19 Hz at approximately 1.5 to 3.5 seconds. This increasing amplitude represents the wing chordwise response due to an 18.7 Hz swashplate input designed to excite the pylon yaw mode – the associated swashplate controller input voltage amplitude is provided in Fig. 20c, see black line. There is a clear time-correlation between the increase in the excitation input signal and the amplitude of the bending moment in the 19 Hz range. Another major feature of the TRF is the 1P forced response at 12.1 Hz that is visible throughout the entire signal. Lastly, an intermittent response of the chord mode can be seen at 7.8 Hz – the swashplate-motion-produced excitation force

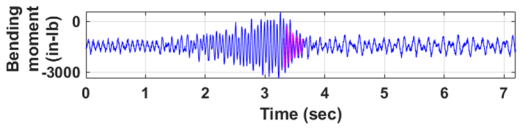

(a) Wing chordwise bending response time history (blue) and reconstructed damped response (purple).

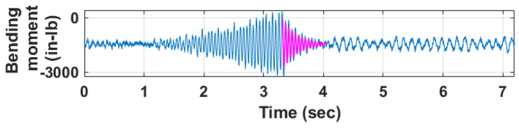

(d) Wing chordwise bending response time history, (blue) and reconstructed damped response (purple); 1P notch filter.

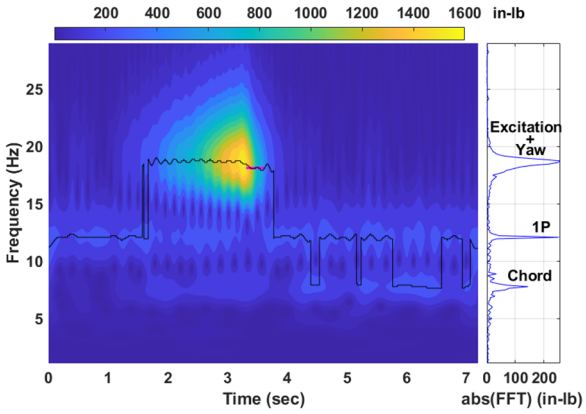

(b) Stockwell transform time-frequency representation (left) and FFT of signal (right). Instantaneous maximum response (black), data used for damping analysis (purple).

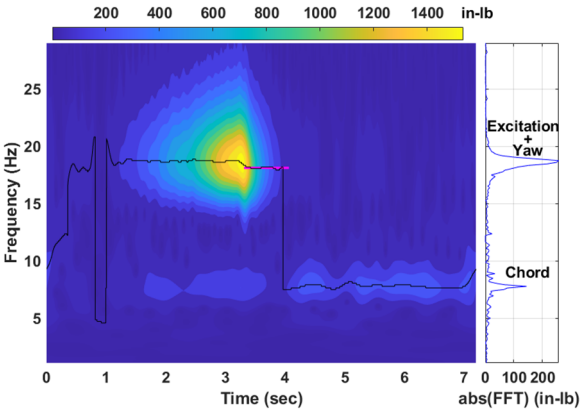

(e) Stockwell transform time-frequency representation (left) and FFT of signal (right). Instantaneous maximum response (black), data used for damping analysis (purple); 1P notch filter.

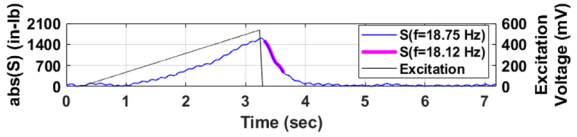

(c) Amplitude of Stockwell transform at excitation and yaw response frequencies and amplitude of excitation input signal time history.

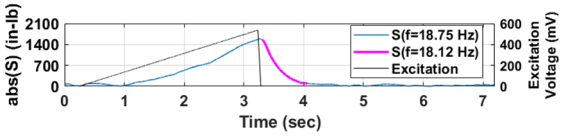

(f) Amplitude of Stockwell transform at excitation and yaw response frequencies and amplitude of excitation input signal time history; 1P notch filter.

Figure 20. Yaw excitation time history and Stockwell transform analysis, V = 135 kts, Ω=727 RPM, 4k pitch spring.

appears to also excite the chord mode. To the right of the TFR is the of the signal FFT (computed by time-averaging the S-transform) plotted with the amplitude on the abscissa and frequency on the ordinate (to match the TFR). It should be noted that the amplitude of the FFT at the frequency of excitation (18.7 Hz) is much smaller than the peak instantaneous amplitude in the TFR – 257 vs. 1605 in-lbf, respectively. This difference is due to the underlying assumption of an FFT that the signal is stationary – constant frequency content across the entire time history – while the S-transform localizes the signal amplitude in time. This property of the S-transform can be used to identify the peak response at any moment in time, which was identified and the frequency of the peak response provided as a black line in Fig. 20b. The majority of the time history is dominated by the 1P forced response, except during the excitation period. The peak response during the excitation period occurs at a frequency of 18.7 Hz. Once the excitation is cut off at approximately 3.3 seconds, the peak response drifted to a lower frequency of 18.1 Hz, indicating that the frequency of the excitation signal did not match the target modal frequency but was sufficiently close to excite it.

One of the shortcomings of the S-transform, as well as other time-frequency methods, is that the energy distribution of the signal is spread over a range of frequencies. This artifact is evident in the TRF presented in Fig. 20b, where the 18.7 Hz model response due to the excitation signal increases the S-transform amplitudes over a wide frequency range. Furthermore, 18.7 Hz energy distribution in this TFR is distorted by its proximity to the 1P signal – this distortion manifests itself as an undulation in the amplitude of the excitation signal. The distortion can affect the identification of the frequency of the peak response (visible as an oscillation in the peak frequency trace at 1.5 to 3 seconds). Therefore, a notch filter is applied to the original time history to remove the 1P signal, see Fig. 20d. The resulting TFR is much smoother (see Fig. 20e), providing a more accurate and consistent identification of the frequency of the peak response and improving the damping calculation by extending the length of the exponentially decaying signal, compare magenta traces in Figs. 20c and 20f.

Statistical selection

Traditional damping analysis such as logarithmic decrement or moving block requires a user to determine the appropriate time segment that they deem represents a damped response after model excitation. Furthermore, the user may need to identify an appropriate bandpass filter range to isolate the frequency of interest, although the actual frequency may be identified automatically in some analyses (Ref. 13). These steps may need to be repeated multiple times until the user considers the results to be correct based on signal reconstruction and engineering judgement. This approach is time-intensive and the results can be affected by personal interpretation and experience.

In the present analysis, a statistical approach is implemented to identify the frequency of the target mode and an appropriate time segment for determining the damping ratio using the S-transform. The basic concept behind the statistical method described below is that the time segment, or window, used to identify the dominant local frequency and to calculate the damping ratio of the signal should provide a consistent dominant frequency and a "high-quality" curve fit of the signal amplitude to determine the damping ratio – in this case, a linear fit of $log_{10}(|S(f_{mode}, t_{segment})|)$, where $|S|$ is the amplitude of the S-transform at frequency f_{mode} within the time range $t_{segment}$. The quality, or appropriateness, of the fit is quantified using the coefficient of determination, R^2, whose value ranges from 0 to 1, where 1 indicates a perfect fit. In the proposed approach, the S-transform is the most-computationally intensive component of the analysis, but only a single calculation of the transform is required to characterize the frequency content of the signal. Varying the time segment length and starting location incurs minimal additional computational cost, since it only requires that the appropriate information is extracted from the S-transform output.

The automated damping determination analysis is conducted in several steps outlined below. To provide insight and clarity of how this analysis identifies the appropriate frequency, time segment, and ultimately the damping ratio, the yaw mode excitation time history provided in Fig. 20 is evaluated as an example, with graphical output from the intermediate steps of this analysis provided in Fig. 21. The process proceeds as follows:

1. Use a test run log or full-signal FFT (Fig. 20e) to identify excitation frequency and use it to define a frequency range to search for the target modal frequency – set to ±1.5 Hz for this analysis. Determine the excitation cut off time (represented by gray vertical dashed line in Fig. 20a at 3.29 sec). S-transform coefficients that are within the defined frequency range and post-excitation time are utilized in the statistical analysis (see Fig. 21a).
2. A time segment of 1 wavelength (based on excitation frequency) is used to determine the local dominant frequency by time-averaging the S-transform amplitude and identifying the peak amplitude. At the identified frequency, the local damping ratio and R^2 of fit for this time segment are calculated. The time segment is moved across the entire post-excitation section of the data point to develop a set of time-varying frequency, damping ratio, and R^2 functions (see Figs. 21b-d, black trace).
3. Vary the time segment length from 1 wavelength to a quarter of post-excitation time, in half cycle increments, and repeat step 2 for each new segment length (see Fig. 21b-d, gray traces).

4. At each time step, identify all overlapping segments from step 3 and calculate the mean and standard deviation of the frequency, damping ratio, and R^2 (see mean values in Fig. 21e-g, standard deviation of R^2 in Fig. 21h; blue traces).
5. At each time step, use mean and standard deviation of frequencies and damping ratios from step 4 to remove outliers whose values fall outside of the standard deviation. Using this reduced set of data at each time step, recalculate the mean for frequency, damping ratio, and R^2 and the standard deviation for R^2 (see means in Fig. 21e-g, standard deviation of R^2 in Fig. 21h; red traces).
6. Calculate an objective function based on the reduced set of R^2 values, $R^2_{reduced}$,

$$J = mean(R^2_{reduced})\left(1 - \sigma(R^2_{reduced})\right)$$

Where $mean(R^2_{reduced})$ is an overall indication of how well the curve fit predicts the exponential decay for all overlapping time segments and the $1 - \sigma(R^2_{reduced})$ is a penalty function that quantifies how much scatter there is in the quality of the curve fits. This time-varying value of J is provided in Fig. 21i.
7. Identify the local maxima of J closest to the end of excitation (highlighted by the filled circle symbol in Fig. 21i). Identify continuous portion of J that remains within X% of this peak value to determine time range for the damping analysis. For the present analysis X is set to 5%. This time segment is used for the final calculation of frequency and damping ratio of the mode. The starting and ending time of this time segment is identified by two vertical magenta-colored lines in Figs. 21b–i.

For the time history presented in Fig. 20, this analysis, graphically represented in Fig. and 21, determined the yaw mode frequency to be 18.12 Hz, and a damping ratio of 3.42% critical.

Results

A comparison of frequency and damping ratios determined using the automated and traditional techniques for the first wing vertical bending, wing in-plane bending, wing torsion, and pylon yaw modes, are provided in Fig. 22a–d. The vertical and in-plane bending mode results (Figs. 22a and 22b), match the traditional approach results well. The yaw mode (Fig. 22c) damping and frequency determined using the automated method generally follow the trends determined using traditional methods, but the damping ratio is slightly higher at lower speeds and trends lower at high tunnel airspeeds. The torsion mode (Fig. 22d), which is typically difficult to analyze, indicates significant scatter in the results for both the automated and traditional techniques, although the automated technique included more data points and suggests clear trends in both frequency and damping ratio.

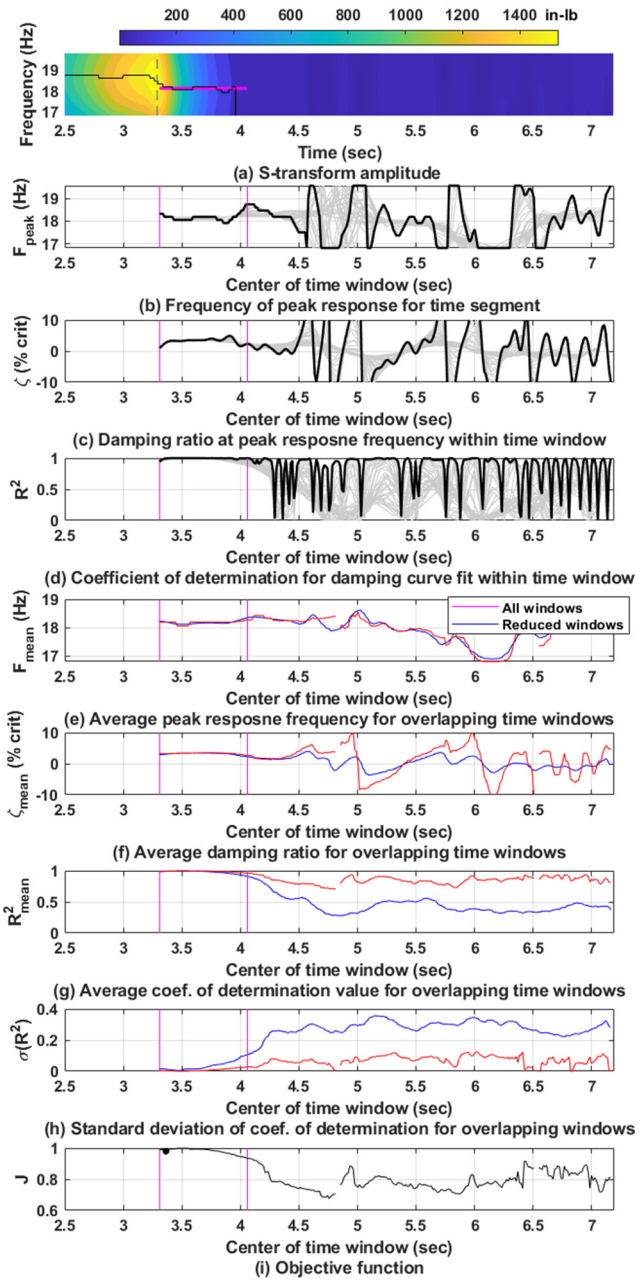

Figure 21. Algorithm output for identifying frequency and damping ratio.

Conclusions

This paper has presented an overview of the TiltRotor Aeroelastic Stability Testbed (TRAST) and the results of the ground vibration testing, excitation and damping, and wind tunnel testing conducted on the testbed. The TRAST, which is a semispan model with an aeroelastically-scaled wing and 8-ft diameter rotor, was designed to conduct fundamental research into the aeroelastic stability phenomenon known as whirl flutter. The results of the tests conducted on the TRAST testbed provide valuable experimental data for the validation of high-fidelity analysis tools for tiltrotor aeroelastic stability,

and for the understanding of the mechanisms contributing to whirl flutter. The results also show that the TRAST testbed is a valuable tool for studying the effect of different design parameters, such as pylon pitch spring stiffness, on the aeroelastic stability of tiltrotor aircraft.

The experimental results obtained from the whirl-flutter testing provide valuable insights into the dynamics of the rotor-wing system. The following key findings can be identified:

- Windmilling was a less stable configuration compared to powered testing.
- Damping as a function of torque indicates a similar trend to previous tests but the windmilling configuration produced approximately 1% lower damping than the powered configuration.
- The fact that in the windmilling configuration the rotor is not disengaged from the nacelle gearbox and wing shaft has potential influence on the amount of damping or energy dissipation of the system.
- The stiffer, 8k pitch spring resulted in lower damping for the wing vertical bending mode compared to the 4k pitch spring. This difference may be due to increased friction with more motion from the softer 4k pitch spring.
- The pitch spring had little impact on the wing in-plane mode.
- The model configuration with the 4k pitch spring and rotor windmilling at 727 RPM displayed signs of instability in the wing vertical bending mode around 170 knots.
- Compared to the damping at a rotor speed of 727 RPM, the damping at a rotor speed of 909 RPM was less stable at multiple velocities but due to limitations the stability boundary was not verified.
- Variation in wind modal damping with temperature and amplitude of motion was identified. This is being addressed for future tests.

Additionally, a new automated approach was described for determining modal frequency and damping in the acquired data. This approach utilizes a nonstationary signal processing method, called the Stockwell transform, combined with statistical methods to identify an appropriate frequency and time segment to determine the modal damping. This new approach compared well with more traditional methods, such as moving block and Prony, that rely more on significant user interaction and engineering judgement.

Overall, these results highlight the importance of carefully selecting the pitch spring stiffness and rotor speed for optimal stability during flight. Future research could investigate additional parameters that affect the dynamics of the rotor-wing system, such as changes in control system or rotor flexibility. The data obtained from the TRAST testbed will be useful for future studies on tiltrotor aeroelastic stability and for the

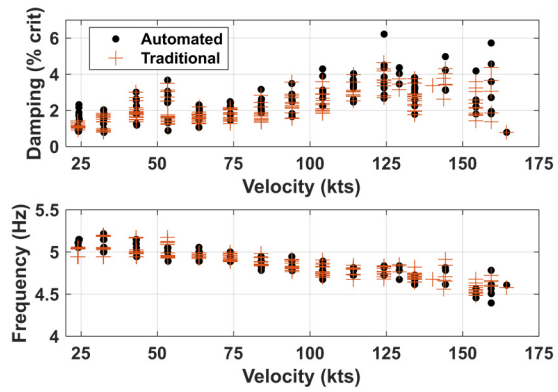

(a) Beam mode

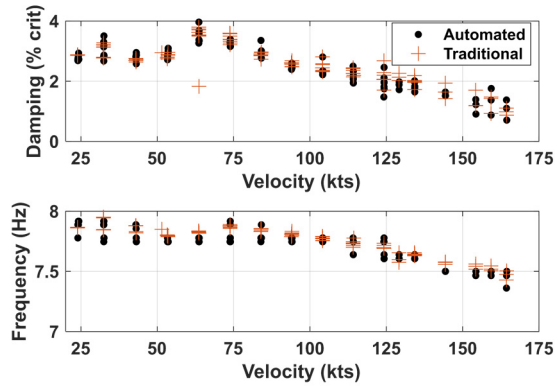

(b) Chord mode

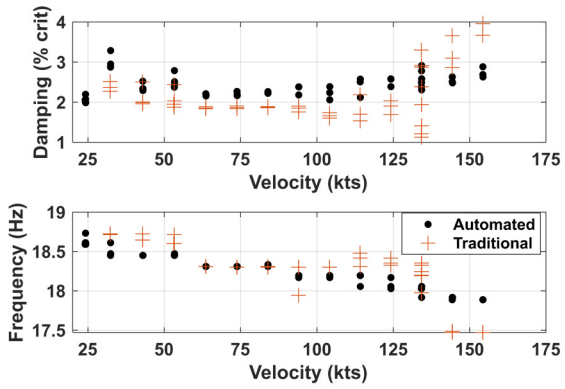

(c) yaw mode

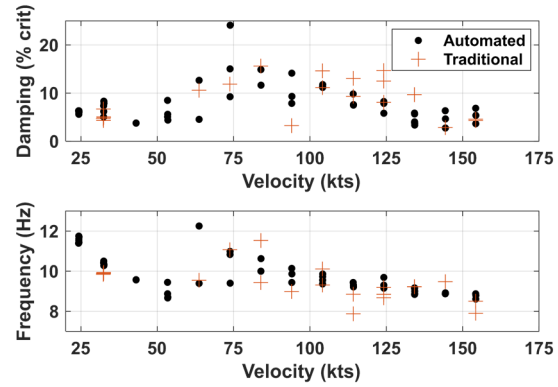

(d) Torsion mode

Figure 22. Comparison of modal frequency and damping ratio, rotor speed of 909 RPM, 4K pitch spring.

design of more advanced tiltrotor aircraft that can achieve higher speeds while maintaining stability. Follow-on testing will hopefully limit some of the model nonlinearities, which will result in a more consistent set of comparisons for rotorcraft comprehensive analysis.

References

1. Reed, W. H. III., "Review of Propeller-Rotor Whirl Flutter," NASA/TR R-264, July 1967.
2. Johnson, W., "Dynamics of Tilting Proprotor Aircraft in Cruise Flight," NASA Technical Note D-7677, May 1974.
3. Kvaternik, R., "An Experimental and Analytical Investigation of Proprotor Whirl-Flutter," NASA Technical Paper 1047, December 1977.
4. Yeager, W., Kvaternik, R., "A Historical Overview of Aeroelasticity Branch and Transonic Dynamics Tunnel Contributions to Rotorcraft Technology and Development," NASA TM-2001-211054/ARL-TR-2564, Hampton, VA, Aug. 2021.
5. Kreshock, A. R., Kang, H., Acree, C. W., and Yeo, H., "Development of a New Aeroelastic Tiltrotor Wind Tunnel Testbed," Proceedings of the AIAA Science and Technology Forum and Exposition (AIAA SciTech 2019), San Diego, CA, January 7-11, 2019.
6. Kreshock, A. R., Thornburgh, R. P., and Wilbur, M. L., "Overview of the TiltRotor Aeroelastic Stability Testbed," Proceedings of the AIAA Science and Technology Forum and Exposition (AIAA SciTech 2022), San Diego, CA, January 3-7, 2022.
7. Kreshock, A. R., Thornburgh, R. P., Kang, H., and Yeo, H., "Pretest Flutter Predictions of the Upcoming Aeroelastic Tiltrotor Wind Tunnel Test," Proceedings of the 76th Annual Forum of the Vertical Flight Society, Virginia Beach, VA, Oct. 6-8, 2020.
8. Piatak, David J.; Kvaternik, Raymond G.; Nixon, Mark W.; Langston, Chester W.; Singleton, Jeffrey D.; Bennett, Richard L.; and Brown, Ross K., "A Wind-Tunnel Parametric Investigation of Tiltrotor Whirl-Flutter Stability Boundaries," 2003 International Forum on Aeroelasticity and Structural Dynamics, Amsterdam, The Netherlands, June 4-6, 2003.
9. Kreshock, A. R., and Thornburgh, R. P., "Ground Vibration Testing of the TiltRotor Aeroelastic Stability Testbed," NASA TM (to be published).
10. Thornburgh, R. P., and Kreshock, A. R., "Finite-Element Structural Modeling of the TiltRotor Aeroelastic Stability Testbed," NASA TM (to be published).
11. Hammond, C. E. and Doggett Jr., R. V., "Determination of Subcritical Damping by Moving-Block/Randomdec Applications," Proceedings of Flutter Testing Techniques Conference, Edwards, CA, Oct 9-10, 1975.
12. Stockwell, R. G., Mansinha, L., and Lowe, R. P., "Localization of the Complex Spectrum: The S-Transform," IEEE Transactions on Signal Processing, vol 44, no.4 April 1996.
13. Sekula, M. K. and Russell, C. R., "Time-Frequency Analysis of Experimental and Analytical Hub Loads of a Rotor Undergoing a Rotor Speed Change," VFS 78th Annual Forum and Technology Display, paper 78-2022-0039, Ft. Worth, TX, May 10-12, 2022, doi: 10.4050/F-0078-2022-17526
14. Kvaternik, Raymond, "Studies in tilt-rotor VTOL aircraft aeroelasticity" Ph. D. Thesis, Case Western Reserve University, 1973.